JACS Au
AN OPEN ACCESS JOURNAL OF THE AMERICAN CHEMICAL SOCIETY

pubs.acs.org/jacsau
Methods/Protocols

DFT-CES2: Quantum Mechanics Based Embedding for Mean-Field QM/MM of Solid−Liquid Interfaces

Taehwan Jang, Seung-Jae Shin, Hyung-Kyu Lim, William A. Goddard, III, and Hyungjun Kim*

Cite This: *JACS Au* 2025, 5, 2047−2058
Read Online

ABSTRACT: The solid−liquid interface plays a crucial role in governing complex chemical phenomena, such as heterogeneous catalysis and (photo)electrochemical processes. Despite its importance, acquiring atom-scale information about these buried interfaces remains highly challenging, which has led to an increasing demand for reliable atomic simulations of solid−liquid interfaces. Here, we introduce an innovative first-principles-based multiscale simulation approach called DFT-CES2, a mean-field QM/MM method. To accurately model interactions at the interface, we developed a quantum-mechanics-based embedding scheme that partitions complex noncovalent interactions into Pauli repulsion, Coulomb (including polarization), and London dispersion energies, which are described using atom-dependent transferable parameters. As validated by comparison with high-level quantum mechanical energies, DFT-CES2 demonstrates chemical accuracy in describing interfacial interactions. DFT-CES2 enables the investigation of complex solid−liquid interfaces while avoiding extensive parametrization. Therefore, we expect DFT-CES2 to be broadly applicable for elucidating atom-scale details of large scale solid−liquid interfaces for multicomponent systems.

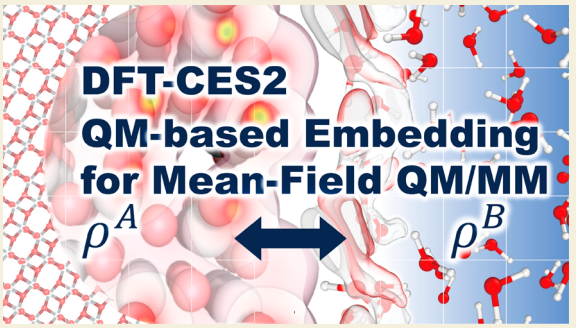

KEYWORDS: *mean-field QM/MM, quantum mechanical embedding method, solid−liquid interfaces, multiscale simulations, surface wettability, ab initio parametrization*

INTRODUCTION

The chemical reactions in heterogeneous catalysis occur at the interface between two different phases of matter. In electrocatalysis, particular emphasis is placed on the solid−liquid interface, which serves as the technological foundation toward a renewable society. To unveil the atom-level details of the microenvironment at the catalytic interface controlling the products, computational methods need to account for the different length and time scales inherent in its heterogeneity. Consequently, first-principles-based multiscale simulation becomes an essential tool for optimizing product selectivity.[1] Here, QM/MM simulations, combining two levels of methods based on quantum mechanics (QM) and classical molecular mechanics (MM), prove advantageous in providing atomistic mechanisms operating at the interfaces.[2−4]

In QM/MM simulations, the total Hamiltonian ($H^{QM/MM}$) is partitioned into components for the QM region (H^{QM}), the MM region (H^{MM}), and their interaction energy ($E_{int}^{QM/MM}$). While determination of the first two terms is straightforward, the accuracy of QM/MM simulations critically depends on the accuracy of the interaction term:

$$H^{QM/MM} = H^{QM} + H^{MM} + E_{int}^{QM/MM} \quad (1)$$

Here, $E_{int}^{QM/MM}$ is typically designed to include van der Waals (vdW) interactions (E_{vdW}) and Coulomb (E_{Coul}) interactions (for example, using an electrostatic embedding method).[5−7]

For the practical application of QM/MM simulations in solid−liquid interfacial systems, involving a considerably large simulation cell, our group has introduced a novel simulation protocol named density functional theory in classical explicit solvents (DFT-CES).[8] Unlike conventional QM/MM simulations that simultaneously evolve QM and MM particles by solving equations of motion derived from $H^{QM/MM}$ in eq 1, DFT-CES involves iterative planewave DFT optimizations (without dynamics) and finite-time molecular dynamics (MD) simulations until a self-consistent solution is achieved. This approach is rooted in a mean-field coupling concept.[9−12] It is noteworthy that these iterations can be understood as optimizing the QM subsystem on the Helmholtz free energy surface.[13]

As an interaction communication channel, DFT-CES utilizes a 3D rectangular grid to provide an accurate and seamless

Received: February 14, 2025
Revised: March 28, 2025
Accepted: April 1, 2025
Published: April 12, 2025

https://doi.org/10.1021/jacsau.5c00176
JACS Au 2025, 5, 2047−2058

description of E_{Coul} between nuclei charge/electron density in the QM region and point charges in the MM region. E_{vdW} relies on a typical pairwise description, with parameters currently adopted from the OPLS-AA force fields[14] for organic systems, which demonstrate notable accuracy in predicting the hydration free energies of small molecules.[8,15] However, to extend the applicability of DFT-CES to solid−liquid interfacial systems, it was necessary to develop new parameter sets for solid−liquid vdW interactions, such as water interaction on carbon[16] or metal surfaces,[17] This was accomplished by fitting parameters to the QM-level binding energy curve of a single liquid molecule on the specified surface.

Despite its success in elucidating various solid−liquid interfaces,[18] the description of $E_{int}^{QM/MM}$ in DFT-CES gives rise to several theoretical and practical challenges. First, the vdW parameters require reparameterization depending on the system of interest. This poses a practical difficulty in applying DFT-CES to a variety of systems. Second, the optimization of the QM subsystem lacks consideration for the cavity confinement effect. This deficiency arises because the Pauli repulsion is described solely by the repulsive vdW interaction defined between QM nuclei and MM atoms, without any dependence on the QM electron density. Moreover, the use of a planewave basis set may exacerbate the undesired electron spillover problem[19,20] for certain systems, although the mean-field coupling that smears the spatial charge distribution in the MM region helps minimize it. Additionally, the electronic polarization response of the MM particles is absent, representing an intrinsic limitation of an electrostatic embedding scheme.

Here, we introduce a new mean-field QM/MM simulation, termed DFT-CES2, designed to address the issues outlined above. DFT-CES2 models the Pauli exchange interaction between QM and MM regions, and mutual polarization is considered at a mean-field coupling level. Notably, DFT-CES2 minimizes the need for extensive reparameterization of the vdW interaction, thereby enhancing the applicability of the method to investigate a broad range of solid−liquid interfaces.

RESULTS AND DISCUSSION

The density functional embedding theory (DFET)[21−23] considers the system partitioned into two parts: A (the embedded region) and B (the environment), which constitute the entire system. Here, the electron density of the entire system is partitioned into two subsystems: $\rho = \rho^A + \rho^B$. This results in the expression of Kohn−Sham (KS) energy, which incorporates the internal energies of subsystems, as well as the interaction term consisting of Coulomb contribution (ΔJ) and nonadditive (nad) exchange (E_x^{nad}), correlation (E_c^{nad}) and kinetic energies (T_s^{nad}):

$$E[\rho] = E^A[\rho^A] + E^B[\rho^B] + E_{int}[\rho^A, \rho^B] \tag{2}$$

$$E_{int} = \Delta J + E_c^{nad} + E_x^{nad} + T_s^{nad} \tag{3}$$

We now approximate subsystem B in a classical limit, describing it as an MM part (i.e., A = QM and B = MM). Using MM, $E^B[\rho^B]$ can be approximated as the force-field (FF) energy; $E^B[\rho^B] := E^{FF}(\{\boldsymbol{r}_b\})$, where $\{\boldsymbol{r}_b\}$ denotes the positions of MM particles.

Nonadditive Correlation Energy

At the limit of weak density overlap between subsystems, such as when there are no chemical bonds across the QM/MM boundary, there exists the long-range correlation energy between nonoverlapping electron densities, commonly known as the London dispersion interaction. This can be recovered by additionally incorporating atom-centered pairwise interactions, which is a common practice in vdW corrected DFT methods. Here, we utilize Grimme's DFT-D3 scheme[24] along with the Becke-Johnson (BJ)-damping function:[25]

$$E_c^{nad} := E_{disp}(\{\boldsymbol{r}_a, \boldsymbol{r}_b\}) = -s \sum_{a\in A, b\in B} \frac{C_{6,ab}}{\boldsymbol{r}_{ab}^{\,6} + f(R_{ab})^6} \tag{4}$$

where $f(R_{ab}) = a_0 R_{ab}^0 + a_1$, and $\{\boldsymbol{r}_a\}$ represents the nuclei positions of the subsystems A. Note that DFT-D3 parametrizes $C_{6,ab}$ and R_{ab}^0 in an *ab initio* manner. The value of $C_{6,ab}$ for each atom is determined using time-dependent DFT calculations with the Casimir-Polder formula,[26,27] and we use the same values. In DFT-D3, R_{ab}^0 is evaluated as $\sqrt{C_{8,ab}/C_{6,ab}}$, where $C_{8,ab}$ is computed recursively from C_6.[28] However, we set R_{ab}^0 as proportional to $(\alpha_b^{iso})^{1/3}$ based on the scaling law between the classical van der Waals radius and the atomic dipole polarizability, α_b^{iso},[29] since we confirmed a strong correlation between R_{ab}^0 in DFT-D3 and $(\alpha_b^{iso})^{1/3}$ (R^2 = 0.996; see Figure S1). Meanwhile, s, a_0 and a_1 are free parameters dependent on the method (e.g., DFT functionals) used, and these global parameters are optimized for our QM/MM simulations below.

Nonadditive Exchange and Kinetic Energies

Intermolecular exchange repulsion, which is a purely quantum-mechanical effect, arises when overlapping molecular orbitals are antisymmetrized to satisfy the Pauli exclusion principle. This orthogonalization process depletes electrons in the wave function overlap region, resulting in an increase in energy, termed Pauli repulsion energy (E_{Pauli}).[30] E_{Pauli} is well described by the Hartree−Fock (HF) interaction energy between two closed-shell wave functions,[31] which is partitioned into the classical Coulombic interaction between the two separated wave functions and E_{Pauli}.[30] Comparing this with eq 3 of DFET, one finds that $E_x^{nad} + T_s^{nad} = E_{Pauli}$, since the correlation energy is absent in the HF theory. This aligns with the previous view that the Pauli potential is primarily governed by kinetic energy,[32−34] while also incorporating a contribution from the exchange-energy functional term.

On the other hand, previous studies correlated E_{Pauli} to the square of nonorthogonalized wave function overlap[30,35−38] or electron density overlap.[39,40] Based on this, we express E_{Pauli} as proportional to the size of the density overlap: $E_{Pauli} = C \int d^3\boldsymbol{r}\, \tilde{\rho}^A(\boldsymbol{r})\, \tilde{\rho}^B(\boldsymbol{r})$ (C being a proportional constant.) Here, $\tilde{\rho}^{A(B)}$ represents the electron density of unperturbed (nonorthogonalized) orbitals, distinguishing it from the density of orthogonalized orbitals, $\rho^{A(B)}$.

To apply this idea in QM/MM modeling, we approximate the electron density of the MM part (B) using Gaussian functions centered at MM particle positions; $\tilde{\rho}^B = \sum_{b\in B} \tilde{a}_b\, g(\boldsymbol{r} - \boldsymbol{r}_b; \sigma_b)$, where $\tilde{a}_b$ is the scaling parameter and $g(\boldsymbol{r}; \sigma)$ is the Gaussian function centered at zero with variance σ. Here, the size of the electron density (σ_b) is approximated based on an isotropic atomic polarizability of the MM particle (α_b^{iso}), using the relation of $\alpha_b^{iso}/4\pi\epsilon_0 = 3\sqrt{\pi/2}\,\sigma_b^{\,3}$.[41] This yields the Pauli energy expression of

$$E_x^{nad} + T_s^{nad} := E_{Pauli}[\tilde{\rho}^A(\boldsymbol{r})] = \int d^3\boldsymbol{r}\, v_{Pauli}(\boldsymbol{r}_b; \sigma_b)\, \tilde{\rho}^A(\boldsymbol{r}) \tag{5}$$

https://doi.org/10.1021/jacsau.5c00176
JACS Au 2025, 5, 2047−2058

$$v_{\mathrm{Pauli}}(\boldsymbol{r}_b;\, \sigma_b) = \sum_{b\in B} a_b g(\boldsymbol{r} - \boldsymbol{r}_b;\, \sigma_b) \tag{6}$$

where the atom-dependent parameter of $a_b \equiv C\tilde{a}_b$, will be parametrized using *ab initio* energetics; *vide infra*.

Coulomb Interaction

ΔJ corresponds to the classical Coulomb interaction between two subsystems. Since the point charges of MM particles are typically chosen to reproduce the electrostatic potential of molecules in the MM region (e.g., electrostatic potential-derived charges), we model ΔJ as the interaction of the unperturbed electron density ($\tilde{\rho}^A$) and nuclei charges (z_a) in A with the distributed point charges $\{q_b\}$ in B. Although there is some ambiguity in choosing either $\tilde{\rho}^A$ or ρ^A, our simulations indicate that this choice affects ΔJ by only about 2% (see Table S1).

The use of fixed-point charges to describe the electrostatics of subsystem B neglects the electronic polarization effect in the MM region. To address this, we incorporate both first-order electrostatic and second-order induction energies to ΔJ;

$$\Delta J \coloneqq E_{\mathrm{Coul}}[\tilde{\rho}^A] = E_{\mathrm{elec}}[\tilde{\rho}^A] + E_{\mathrm{ind}}[\tilde{\rho}^A] \tag{7}$$

$$E_{\mathrm{elec}}[\tilde{\rho}^A] = \int \mathrm{d}\boldsymbol{r}^3\, v_{\mathrm{q}}^B(\boldsymbol{r})\{\rho_{\mathrm{nuc}}^A(\boldsymbol{r}) - \tilde{\rho}^A(\boldsymbol{r})\} \tag{8}$$

where $\rho_{\mathrm{nuc}}^A = \sum_{a\in A} z_a \delta(\boldsymbol{r} - \boldsymbol{r}_a)$, so that $\rho_{\mathrm{nuc}}^A - \tilde{\rho}^A(\boldsymbol{r})$ corresponds to the total charge density of the QM subsystem (ρ_{nuc}^A). Note that we adopt an electron-is-positive charge convention, resulting in the subtraction of ρ^A from $\rho_{\mathrm{nuc}}^A(\boldsymbol{r})$. $v_q^B(\boldsymbol{r}) = \sum_{b\in B} q_b/|\boldsymbol{r} - \boldsymbol{r}_b|$ is the electrostatic potential generated by $\{q_b\}$ in B.

$$E_{\mathrm{ind}}[\tilde{\rho}^A] = -\frac{1}{2}\int \mathrm{d}\boldsymbol{r}^3\, v_{\mathrm{bq}}(\boldsymbol{r})\{\rho_{\mathrm{nuc}}^A(\boldsymbol{r}) - \tilde{\rho}^A(\boldsymbol{r})\} \tag{9}$$

By plugging eqs 8 and 9 into eq 7, we obtain

$$E_{\mathrm{Coul}}[\tilde{\rho}^A] = \int \mathrm{d}\boldsymbol{r}^3\, v_{\mathrm{Coul}}(\boldsymbol{r})\{\rho_{\mathrm{nuc}}^A(\boldsymbol{r}) - \tilde{\rho}^A(\boldsymbol{r})\} \tag{10}$$

where $v_{\mathrm{Coul}} \equiv v_q^B - v_{\mathrm{bq}}/2$.

We note that eq 9 accounts only for mutual polarization occurring across the QM/MM boundary while neglecting polarization effects among MM particles. Polarizable force fields (FFs) such as AMOEBA,[42] RexPoN,[43] and MB-pol[44] can address these missing electronic polarization effects in the MM subsystem, which arise from the use of a fixed-point charge scheme. However, this approach, known as the polarizable embedding scheme, often leads to a substantial increase in computational cost and requires extensive parameter reoptimization.

Mean-Field Coupling

As shown in eqs 4, 5, and 10, all terms constituting E_{int} are now expressed in a way that excludes any explicit dependence on ρ^B for the classical treatment of the subsystem B. These equations lead to the following expression for the terms consisting of the QM/MM total Hamiltonian of DFT-CES2 as

$$H^{\lambda}[\rho^A] = H^{\mathrm{QM}}[\rho^A] + H^{\mathrm{MM}} + E_{\mathrm{int},\lambda}^{\mathrm{QM/MM}}[\rho^A] \tag{11}$$

$$H^{\mathrm{QM}}[\rho^A] = \sum_{a\in A} \frac{\boldsymbol{p}_a^{\,2}}{2m_a} + E^A[\rho^A;\, \{\boldsymbol{r}_a\}] \tag{12}$$

$$H^{\mathrm{MM}} = \sum_{b\in B} \frac{\boldsymbol{p}_b^{\,2}}{2m_b} + E^{FF}(\{\boldsymbol{r}_b\}) \tag{13}$$

$$E_{\mathrm{int},\lambda}^{\mathrm{QM/MM}}[\rho^A] = E_{\mathrm{disp}} - \int \mathrm{d}^3\boldsymbol{r}\, v_{\mathrm{emb}}^{\lambda}\rho^A + E_{\mathrm{nuc}} + E_0 \tag{14}$$

where $v_{\mathrm{emb}}^{\lambda} = v_{\mathrm{Coul}} - \lambda v_{\mathrm{Pauli}}$, $E_{\mathrm{nuc}} = \int \mathrm{d}^3\boldsymbol{r}\, v_{\mathrm{Coul}}\rho_{\mathrm{nuc}}^A$, and $\lambda = 1$ (the reason for introducing λ is provided below). Since eqs 5 and 10 are written in terms of $\tilde{\rho}^A$, we introduce $\Delta\rho^A(\boldsymbol{r}) \equiv \rho^A - \tilde{\rho}^A$ and $E_0 = \int \mathrm{d}^3\boldsymbol{r}\, v_{\mathrm{emb}}\Delta\rho^A$ to express eq 14 in terms of ρ^A. We then formally write the Helmholtz free energy functional as

$$A^{\lambda}[\rho^A,\, \{\boldsymbol{r}_a\}] = -k_{\mathrm{B}}T\, \ln \int \mathrm{e}^{-\beta H^{\lambda}}\, \mathrm{d}\Omega \tag{15}$$

where Ω denotes the integration for the subphase space spanned by $\{\boldsymbol{r}_b\}$. Equation 15 provides the theoretical foundation to variationally optimize the electron density and the structure of the QM subsystem [i.e., ρ^A and $\{\boldsymbol{r}_a\}$, respectively] by minimizing $A[\rho^A,\{\boldsymbol{r}_a\}]$. We optimize ρ^A by including a mean embedding potential $\langle v_{\mathrm{emb}}(\boldsymbol{r})\rangle$ during electronic self-consistent-field (SCF) cycles, and $\{\boldsymbol{r}_a\}$. That is, the structure can be optimized by adding a mean atomic force $\langle \boldsymbol{f}_a^{\mathrm{atom}}\rangle$ to each atom during the DFT geometry optimization steps. Here, $\langle \ldots \rangle = \int (\ldots)\, \mathrm{e}^{-\beta H}\, \mathrm{d}\Omega$ and $\boldsymbol{f}_a^{\mathrm{atom}}$ is the atomic force exerted on the nucleus a by the MM particles via the Coulomb and dispersion interactions (Supporting Note 1).

The variationally optimized ρ^A defines the total energy of the QM/MM system, as given in eq 11, except for the E_0 term, which depends on $\Delta\rho^A$. Since v_{Pauli} is the potential that minimizes the density overlap between A and B by penalizing it, the electron density optimized without including v_{Pauli} can be considered the electron density $\tilde{\rho}^A$ before enforcing the orbital orthogonality. We therefore separately obtain $\tilde{\rho}^A$ by variationally minimizing $A^{\lambda=0}$, where the v_{Pauli} is switched off by setting $\lambda = 0$. We then compute $\Delta\rho^A = \rho^A - \tilde{\rho}^A$ to obtain E_0, and subsequently the total energy expression in eq 11.

During the MD simulation, the presence of the QM subsystem exerts an external force on the MM particle b, $\boldsymbol{f}_b^{\mathrm{ext}}$, consisting of Coulomb ($\boldsymbol{f}_b^{\mathrm{Coul}}$) (given by the sum of first-order electrostatic and second-order induction forces, i.e., $\boldsymbol{f}_b^{\mathrm{elec}} + \boldsymbol{f}_b^{\mathrm{ind}}$), Pauli ($\boldsymbol{f}_b^{\mathrm{Pauli}}$), and dispersion ($\boldsymbol{f}_b^{\mathrm{disp}}$) forces, which can be obtained by computing the gradient of the interaction energy, $-\nabla_{\boldsymbol{r}_b} E_{\mathrm{int}}^{\mathrm{QM/MM}}$; see the Supporting Note 2 for full expressions.

Grid-Based Coupling

To implement the quantum mechanics-based QM/MM embedding scheme, we need to numerically evaluate $\langle v_{\mathrm{emb}}(\boldsymbol{r})\rangle$. This involves employing three-dimensional real-space rectangular grids, where the grid spacing h is usually of subangstrom order, to numerically sample $\langle v_{\mathrm{q}}^B(\boldsymbol{r})\rangle$, $\langle v_{\mathrm{bq}}(\boldsymbol{r})\rangle$, and $\langle v_{\mathrm{Pauli}}(\boldsymbol{r})\rangle$ from the MD trajectory of the MM subsystem.

For the electrostatic potential term, we compute the trajectory-averaged density of MM point charges,

$$\langle \rho_{\mathrm{q}}^B(\boldsymbol{r})\rangle = \left\langle \sum_{b\in B} q_b \delta(\boldsymbol{r} - \boldsymbol{r}_b) \right\rangle \tag{16}$$

which is linked with $\langle v_{\mathrm{q}}^B(\boldsymbol{r})\rangle$ through the Poisson equation: $\nabla^2\langle v_{\mathrm{q}}^B(\boldsymbol{r})\rangle = -4\pi\langle \rho_{\mathrm{q}}^B(\boldsymbol{r})\rangle$.

To evaluate $\langle v_{\mathrm{bq}}\rangle$, we define an induced point dipole of $\boldsymbol{d}_b(\boldsymbol{r}) = (d_b^x,\, d_b^y,\, d_b^z) = \alpha_b^{\mathrm{iso}}\nabla v_q^A(\boldsymbol{r})$, yielding $\langle \rho_{\mathrm{bq}}\rangle = -\nabla\cdot\langle \boldsymbol{P}\rangle = -\nabla\cdot\langle \sum_{b\in B}\boldsymbol{d}_b(\boldsymbol{r})\delta(\boldsymbol{r} - \boldsymbol{r}_b)\rangle$. Using the central differencing scheme of the first-order finite difference method, that is,

https://doi.org/10.1021/jacsau.5c00176
JACS Au 2025, 5, 2047−2058

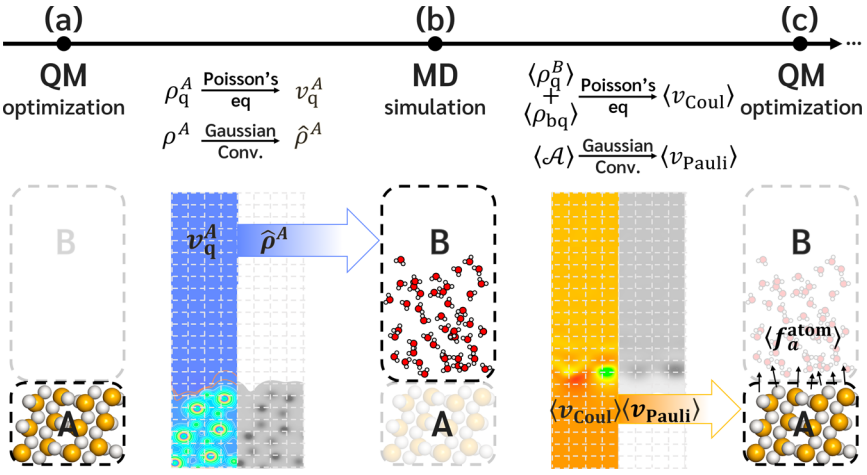

Figure 1. Overall computational procedure of DFT-CES2. (a) DFT calculation is initially performed for the QM subsystem (denoted as A) in a vacuum, generating the electron density (ρ^A) and total charge density (ρ_q^A). Using a fast Fourier transform (FFT)-based Poisson solver, the electrostatic potential (v_q^A) is computed from ρ_q^A on a 3D grid, and the Gaussian-convoluted electron density ($\hat{\rho}^A$) is computed from ρ^A on another 3D grid. These two grid files are then transferred to the MD code. (b) During the subsequent MD simulation, the grid files are linearly interpolated at the positions of the MM particles to compute the external force (f_b^{ext}) based on their interaction with the QM subsystem. MD simulations are performed to compute trajectory-averaged distributions of $\langle\rho_q^A\rangle$, $\langle\rho_{bq}\rangle$, and $\langle\mathcal{A}^s\rangle$ on 3D grids. $\langle\mathcal{A}^s\rangle$ is convoluted with the Gaussian function to compute $\langle v_{Pauli}\rangle$ using eq 19 via postprocessing. The grid files of $\langle\rho_q^B\rangle$, $\langle\rho_{bq}\rangle$, and $\langle v_{Pauli}\rangle$ are transferred to the subsequent DFT code. During MD, the mean atomic force, $\langle f_a^{\text{atom}}\rangle$, exerted on the QM nuclei is also calculated and transferred to the DFT code. (c) The DFT code reads $\langle\rho_q^B\rangle + \langle\rho_{bq}\rangle$ and compute $\langle v_{Cauli}\rangle$ using a built-in Poisson solver. It then adds the embedding potential, $\langle v_{emb}\rangle = \langle v_{Pauli}\rangle + \langle v_{Coul}\rangle$, to the Hartree potential during the self-consistent field (SCF) cycles for optimizing ρ^A. Geometry optimizations are performed under the influence of external atomic forces of $\langle f_a^{\text{atom}}\rangle$. The DFT-computed ρ^A and $\langle\rho_q^A\rangle$ are updated, and the mean-field QM/MM iteration continues until the DFT energy converges within the predefined threshold value (default value is 0.1 kcal/mol).

$\partial_\alpha f(\boldsymbol{r}) = [f(\boldsymbol{r}+\boldsymbol{g}_\alpha) - f(\boldsymbol{r}-\boldsymbol{g}_\alpha)]/2h$ (where $\alpha \in \{x, y, z\}$), we obtain

$$\langle\rho_{bq,\alpha}\rangle = -\left\langle \sum_{b\in B} d_b^\alpha \frac{\delta(\boldsymbol{r}-\boldsymbol{r}_b+\boldsymbol{g}_\alpha) - \delta(\boldsymbol{r}-\boldsymbol{r}_b-\boldsymbol{g}_\alpha)}{2h} \right\rangle \tag{17}$$

$$\langle\rho_{bq}\rangle = -\sum_{\alpha\in\{x,y,z\}} \langle\rho_{bq,\alpha}\rangle \tag{18}$$

Here, $\boldsymbol{g}_x = (h, 0, 0)$, $\boldsymbol{g}_y = (0, h, 0)$, $\boldsymbol{g}_z = (0, 0, h)$, and d_b^α is the α-directional component of $\boldsymbol{d}_b(\boldsymbol{r} = \boldsymbol{r}_b)$ Finally, we obtain $\langle v_{bq}\rangle$ by solving the Poisson equation: $\nabla^2\langle v_{bq}(\boldsymbol{r})\rangle = -4\pi\langle\rho_{bq}\rangle$.

The Pauli repulsion potential, defined in eq 6, can be rewritten using the characteristics of the delta function, $v_{Pauli}(\boldsymbol{r}) = \sum_{b\in B}\int d^3\boldsymbol{r}' a_b g(\boldsymbol{r}-\boldsymbol{r}';\sigma_b)\,\delta(\boldsymbol{r}'-\boldsymbol{r}_b)$. Here, we re-label the MM particle index b using two indices, s and i_s. The index s labels different atomic species that share the same a_b and σ_b, which we now denote as a_s and σ_s, respectively, while i_s labels different atoms within the same species s. The summation over b is replaced with a double summation over s and i_s, i.e., $\sum_{b\in B}(\ldots) = \sum_s\sum_{i_s}(\ldots)$. This leads to

$$\langle v_{Pauli}(\boldsymbol{r})\rangle = \sum_s v_{Pauli,s}(\boldsymbol{r}) \tag{19}$$

where

$$v_{Pauli,s}(\boldsymbol{r}) = \int d^3\boldsymbol{r}'\langle\mathcal{A}^s(\boldsymbol{r}')\rangle g(\boldsymbol{r}-\boldsymbol{r}';\sigma_s) \tag{20}$$

$$\mathcal{A}^s(\boldsymbol{r}) = a_s\left\langle \sum_{i_s}\delta(\boldsymbol{r}-\boldsymbol{r}_{i_s})\right\rangle \tag{21}$$

Thus, we compute the species-dependent atomic number density using the MD trajectory, scale it by a_s, so that obtain $\langle\mathcal{A}^s(\boldsymbol{r})\rangle$. We then convolve it with $g(\boldsymbol{r}-\boldsymbol{r}';\sigma_s)$ in Fourier-transformed space to obtain the species-dependent $v_{Pauli,s}(\boldsymbol{r})$. Finally, the summation of $v_{Pauli,s}(\boldsymbol{r})$ over different atom species yields $\langle v_{Pauli}(\boldsymbol{r})\rangle$.

Consequently, $\langle v_{emb}(\boldsymbol{r})\rangle$ can be calculated by evaluating $\langle\rho_q^B(\boldsymbol{r})\rangle$, $\langle\rho_{bq}\rangle$, and $\langle\mathcal{A}^s(\boldsymbol{r})\rangle$, as defined in eqs 16, 18, and 21, respectively. All of these quantities have the form of $\langle\sum_{b\in B}c\delta(\boldsymbol{r}-\boldsymbol{r}_b)\rangle$ (where c is a scalar value). To sample them from the MD trajectory, $\delta(\boldsymbol{r}-\boldsymbol{r}_b)$ is smoothed using a hat function with the width of h, distributing the single scalar value of c into 8 nearby grid points around $\boldsymbol{r}_b$ (Figure 1 and Figure S2, and Supporting Note 3). Further technical details are found in our previous publication on the original DFT-CES.[8]

Setting up the Simulation

We implemented DFT-CES2 by modifying two open-source programs, Quantum Espresso (QE) version 6.3 for the planewave DFT[45] and Large-scale Atomic/Molecular Massively Parallel Simulator (LAMMPS) version 11 Aug 2017 for the MD.[46]

The modified QE subroutines read two grid files storing $\langle\rho_q^B\rangle + \langle\rho_{bq}\rangle$ and $\langle v_{Pauli}\rangle$ in the Gaussian cube format.[47] This functionality can be switched on by appending an input command of *dft_ces = .true.* and providing the locations of grid files of $\langle\rho_q^B\rangle + \langle\rho_{bq}\rangle$ and $\langle v_{Pauli}\rangle$ using the cards of *rho_ces* and *pauli_rep_ces*, respectively. Then, QE numerically solves the Poisson equation to obtain $\langle v_{Coul}\rangle$ using $\langle\rho_q^B\rangle + \langle\rho_{bq}\rangle$, and appends $\langle v_{Coul}\rangle$ and $\langle v_{Pauli}\rangle$ to the Hartree potential during DFT calculations. Also, the mean atomic forces of $\langle f_a^{\text{atom}}\rangle$, which are averaged over the MD simulation run, are applied to the structure optimization of the DFT calculation using the card of *atomic_forces* as implemented in the original QE.

https://doi.org/10.1021/jacsau.5c00176
JACS Au 2025, 5, 2047−2058

We additionally need to include the input commands of *plot_num = 11* and *plot_num = 0* to print out the electrostatic potential, v_q^A, and the electron density, ρ^A, of the QM subsystem, respectively. Once these are printed out after the DFT calculation, we then generate Gaussian-convoluted electron densities of the QM subsystem, $\hat{\rho}^A(\boldsymbol{r}'; \sigma_b)$, as defined in eq (S22), in an *a posteriori* manner. It is noted that the number of $\hat{\rho}^A(\boldsymbol{r}'; \sigma_b)$ grids is determined by the number of atom types in the MM subsystem, which are differentiated by the different σ_b values.

Grid files storing v_q^A and $\hat{\rho}^A(\boldsymbol{r}'; \sigma_b)$ should be provided to the subsequent MD simulation to compute external forces exerted on the MM particles, as defined in eqs (S17), (S20), and (S23). To enable this, we implemented a *grid* input command in LAMMPS, enabling it to read and write grid files. The *grid* command enables not only reading the v_q^A and $\hat{\rho}^A(\boldsymbol{r}'; \sigma_b)$ grids, but also sampling and time-averaging from MD trajectories various distributed densities of $\langle \rho_q^B \rangle$, $\langle \rho_{bq} \rangle$, and $\langle \mathcal{A}^s \rangle$, which are defined in eqs 16, 18, and 21, respectively. Additionally, we implemented a new fix style of *gridforce* to compute the external forces acting on the MM particle by performing on-the-fly trilinear interpolation of the grid data, and modified the *fix_modify* command to update the corresponding energy term. We also introduced a new *pair_style* of *bjdisp* to compute the pairwise interaction with the functional form of eq 4.

The iteration between DFT and MD simulations is carried out using a custom bash script, *qmmm_dftces2.sh*, where the paths for the QE and LAMMPS executables, the convergence criterion, and locations of grid files need to be specified by the user. Detailed usage of the bash script and syntax for the new input commands in QE and LAMMPS are provided in Figures S3–S6 of the Supporting Information. Code wrappers for QE and LAMMPS, the bash script for the iteration, and example input files are available at the following GitHub link: github.com/dft-ces/dft-ces2.

Universal Atom-Dependent Parameters

To optimize the atom-dependent repulsion parameters, a_b, defined in eq 6, we analyzed the intermolecular interaction of Ar with various small molecules (N_2, O_2, and S_2 for the parameters of N, O, and S, respectively; H_2O for the parameters of H; and a benzene for the parameters of C). We calculated the binding energy curves at the Hartree–Fock (HF) level, ΔE_b^{HF}, which consists of electrostatic and Pauli repulsion energies, with no contribution from dispersion interactions due to the lack of correlation energy. The α_b^{iso} values for each atomic species in molecules were determined from the time-dependent DFT calculations[48] (Table 1), and that of each atomic quantity in transition metal oxides were calculated using the self-consistent screening/fractionally ionic (SCS/FI) approach[49] (see Figure S7). The optimized set of a_b for H, N, O, C, and S results in a close match between ΔE_b^{HF} and the DFT-CES2 binding energy with no dispersion contribution (Figure 2 and Figure S8; see the Supporting Note 4). Further parametrization for alkali metal cations (Figure S9), halide anions (Figure S10), and rare gases (Figure S11) has been performed, which are summarized in Table 1.

The C6 parameters for E_{disp} were determined using Grimme's DFT-D3 scheme.[50] To avoid additional computational overhead from the on-the-fly determination of C6 parameters for molecules in the condensed phase, the atomic C6 parameters were calculated using a single isolated molecule since these values are not significantly affected by the noncovalent interactions.

Table 1. Atom-Dependent Repulsion Parameter (a_b) and Isotropic Atomic Polarizability (α_b^{iso}) for Each Atom Species[a]

Atom species	a_b	α_b^{iso}
H	1.381	1.693
O	15.56	5.20
N	10.51	7.25
S	3.39	19.5
C	5.15	11.7
Li^+	11.30	0.193
Na^+	24.82	0.93
K^+	23.51	5.05
Rb^+	19.26	8.32
Cs^+	11.23	15.0
He	23.78	1.38
Ne	22.01	2.67
Ar	11.08	11.1
Kr	7.617	16.8
Xe	4.532	27.2
F^-	2.600	15.0
Cl^-	2.694	30.3
Br^-	2.175	42.8
I^-	1.938	61.7

[a]The values are given in atomic unit of $E_h \cdot a_0^3 e^{-2}$ for a_b and a_0^3 for α_b^{iso}.

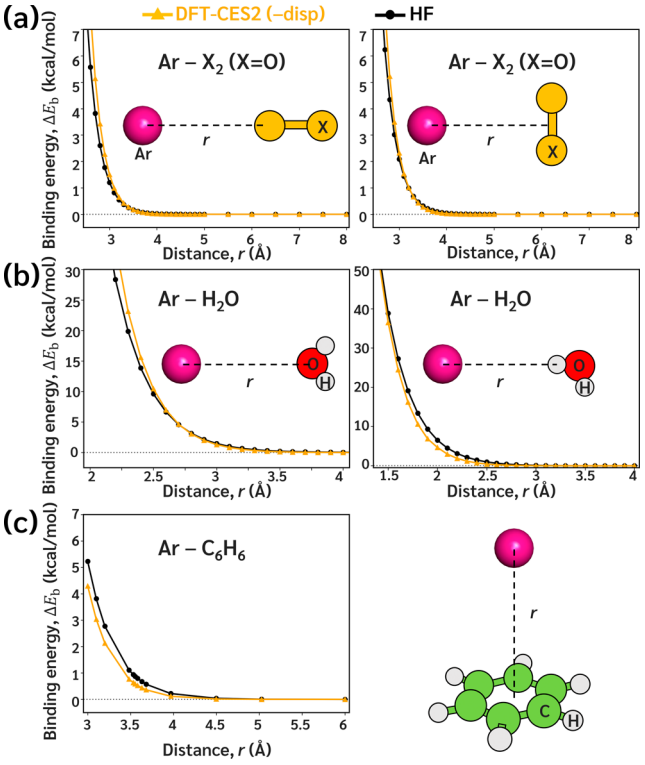

Figure 2. Optimization of atom-dependent repulsion parameter, a_b. (a) The a_b parameter for O is optimized to reproduce the Hartree–Fock (HF) binding energy of Ar and O_2. The same procedure is repeated for Ar–N_2 and Ar–S_2 to obtain a_b parameter for N and S, respectively (Figure S5). (b) While maintaining the a_b parameter for O as optimized for Ar–O_2, the a_b parameter for H is optimized to reproduce the HF binding energy of Ar and H_2O. (c) While maintaining the a_b parameter for H as optimized for Ar–H_2O, the a_b parameter for C is optimized to reproduce the HF binding energy of Ar and benzene.

https://doi.org/10.1021/jacsau.5c00176
JACS Au 2025, 5, 2047–2058

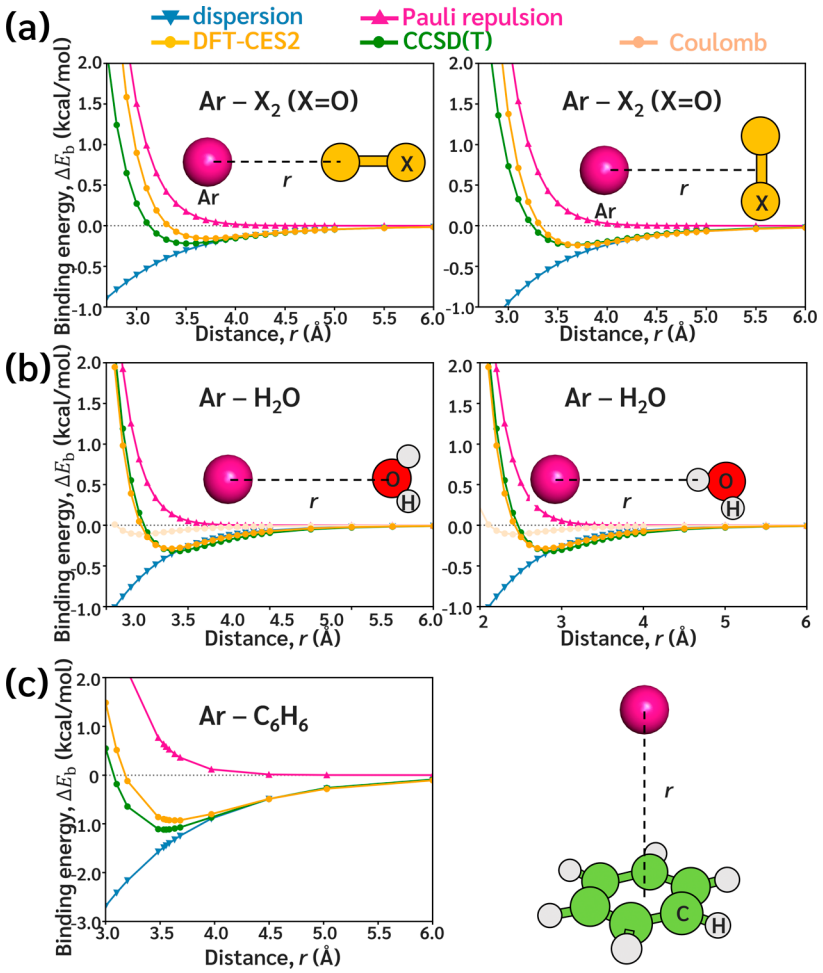

Figure 3. Optimization of scaling parameters of dispersion energy. The parameters of s, a_0 and a_1 of E_{disp} are optimized to reproduce the CCSD(T) binding energies of (a) Ar and O_2, (b) Ar and H_2O, and (c) Ar and benzene. Ar–N_2 and Ar–S_2 cases are shown in Figure S9.

To determine the scaling parameters s, a_0 and a_1 of E_{disp} (see eq 4), we obtained the interaction curves of Ar with the molecules considered above, but now using CCSD(T) theory, which fully accounts for intermolecular dispersion energy. The DFT-CES2 binding energy was matched to the CCSD(T) interaction energy when $R^0 = \sigma_b$, and s, a_0, and a_1 were set to 1.4, 2.1, and 0, respectively (Figure 3 and Figures S12–S15). We found that the optimized a_b parameters and the scaling parameters of E_{disp} provide a reliable description of noncovalent intermolecular interactions, except in cases involving hydrogen bond interactions with water or hydrogen fluoride. Therefore, we adjusted the C_6 parameter for the H atom of the hydrogen bond donor group in OH and HF by 0.443 au to improve the accuracy (Figure S16).

To confirm the reliability of the optimized parameters in describing noncovalent interactions, we benchmarked DFT-CES2 interaction energies against various CCSD(T)-level interaction energy data sets including A24,[51] S22,[52] and several systems including water in S66[53] and X40.[54] We found that the mean absolute error (MAE) for 94 molecular interactions (46 cases from A24, 38 cases from S22, 8 cases from S66, and 2 cases from X40. See Tables S2–S4) is as small as 0.922 kcal/mol, indicating high accuracy and transferability of the optimized parameters (Figure 4a). Notably, our approach fits the Pauli repulsion parameter for each atomic species without requiring further reparametrization for small organic molecules across diverse chemical environments. In comparison with other QM/MM methods, DFT-CES2 outperforms for the S22 benchmark set and is even comparable to high-level dispersion-corrected DFT results (see Table S5).

As a demonstration of molecule–surface interaction, we benchmarked the nonbond interaction between small molecules and metal surfaces, where DFT-CES2 demonstrated better accuracy than the vdW-corrected DFT (Table S6). Additionally, we compared the DFT-CES2 binding energy curve of a water molecule on a graphene surface to the most reliable vdW-corrected DFT energetics, showing a good agreement (Figure 4b and Table S7).

Simulations of Solid–Liquid Interfaces to Predict Water Contact Angles

The solid–liquid interfacial free energy, which corresponds to the reversible work required to separate two phases (i.e., the work of adhesion, W_{ad}), quantifies the interaction strength for solid–liquid contacts. Using DFT-CES2, we calculated W_{ad} for various surfaces, such as graphene, TiO_2, ZrO_2, and CeO_2. The free energy quantities were determined by finite difference thermodynamic integration (FDTI) methods,[55] while gradually turning off the interaction energy between the solid surface and water. The coupling method of alchemical free energy calculation and DFT-CES2 is summarized in the Supporting Information, and will be described in more detail in our future paper.

https://doi.org/10.1021/jacsau.5c00176
JACS Au 2025, 5, 2047–2058

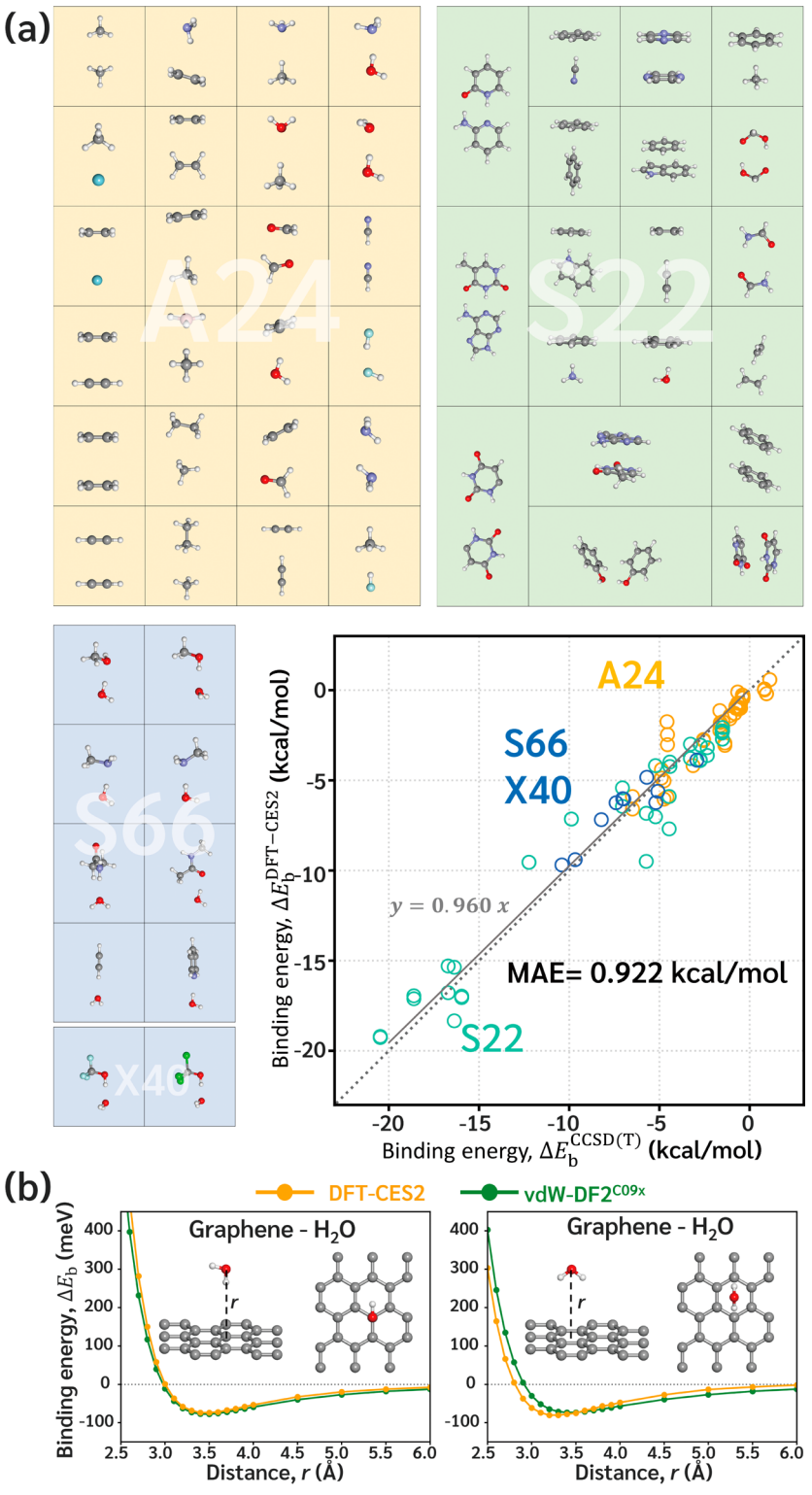

Figure 4. Benchmark of DFT-CES2 interaction energies. (a) A scatter plot benchmarks the DFT-CES2 binding energies for 94 molecular pairs, comprising the A24 (yellow),[50] S22 (green),[51] S66[52] and X40 (blue)[53] sets, against the CCSD(T) binding energies. The energies are listed in Tables S2−S4. The mean absolute error (MAE) is 0.922 kcal/mol, therefore achieving the chemical accuracy. (b) Benchmark of the DFT-CES2 binding energy of water on graphene, as an example of surface-molecule interaction, against the reliable vdW-corrected DFT binding energy. The vdW-DF2^{C09x} functional is employed, which reproduces the quantum Monte Carlo (QMC) binding energy.[62]

Figure 5 presents the DFT-CES2-predicted W_{ad} values, which are also converted into water contact angles, θ_c, using the Young-Dupré equation: $\cos^2 \theta_c/2 = W_{ad}/2\gamma$, where $\gamma = 65.2$ mJ/m^2[56] is the calculated surface tension of TIP4P-Ew water.[57] For the graphene surface, the predicted θ_c is 89.7°, which is in consistent with the experimental value of 84−127°.[58−60] For the oxides, DFT-CES2 predicts θ_c values of 85.0° for TiO_2, 64.1° for ZrO_2, and 69.1° for CeO_2. These predictions are quite comparable to

https://doi.org/10.1021/jacsau.5c00176
JACS Au 2025, 5, 2047−2058

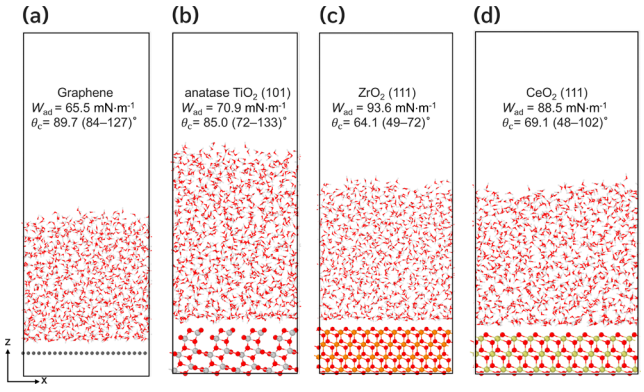

Figure 5. Surface wettability calculations using DFT-CES2. Combining DFT-CES2 with finite difference thermodynamic integration (FDTI) methods enables the calculation of work of adhesion (W_{ad}), which is converted into the water contact angle (θ_c) of (a) graphene, (b) anatase TiO_2 (101), (c) ZrO_2 (111), and (d) CeO_2 (111) surfaces. Water molecules on each surface are shown with oxygen atoms in hydrogen atoms in light gray. The color codes for the surfaces are as follows: dark gray for carbon in (a), dark gray for titanium and red for oxygen in (b), orange for zirconium and red for oxygen in (c), and light green for cerium and red for oxygen in (d). The values in parentheses are experimental data, taken from Fowkes, Morcos, and Wang et al.,[58−60,62] for graphene, Nowak, He, and Wang et al.[63−65] for TiO_2 and ZrO_2, and Azimi and Fu et al.[66,67] for CeO_2.

the experimental results, considering the significant nonideality of the oxide surfaces due to possible defects, polycrystallinity, partial surface oxidation, and other factors, which are expected to have a more substantial effect than on the graphene surface. Thus, based on first-principles-derived transferrable parameters, DFT-CES2 provides a reliable description of the complex interactions at solid−liquid interfaces. However, there is a caveat: the QM/MM approach, including our DFT-CES2, inherits the limitations of current standard force fields, such as the lack of many-body interactions and unavailability to describe the chemical reactions,[61] which remain areas for further development in the field.

A Detailed Guide to DFT-CES2

In this section, we provide a step-by-step explanatory guide that outlines how to construct the system and analyze the DFT-CES2 results to help readers reproduce the DFT-CES2 simulation results and encourage them to apply DFT-CES2 to investigate other systems. As an illustrative example, we consider the graphene system interacting with water molecules.

(Step 1) Construct the Interface and Partitioning It into QM and MM Regions. In DFT-CES2 simulations, a common approach for partitioning a solid−liquid interfacial system is to treat the solid at the QM level and the liquid at the MM level. In this example, we hence simulate graphene using DFT and water molecules using MD. To form the initial structure, we need to build slab geometries for both the solid and liquid and then combine them into a single system. When the initial atomic configurations for the interface system are prepared (*ini_preparation/data.lammps*), we generate a restart file (*ini_preparation/ini.restart*) using the LAMMPS input file (*ini_preparation/make-ini.in*). This restart file is required for the subsequent DFT-CES2 simulation.

(Step 2) Preparation of Input Base Files. Once the initial structure of the solid−liquid interface is constructed, which is stored in the restart file, we prepare the necessary input base files for each subsystem: QE input base files for the solid in the QM region and LAMMPS input base files for the liquid in the MM region.

Examples of QE and LAMMPS input base files for the graphene−water system are provided in the Supporting Information: *base.pp.in* and *base.pw.in* for QE, and *base.in.lammps* for LAMMPS. These input base files contain the QE and LAMMPS simulation protocols, formatted according to the input grammar of each code.

Special attention should be given to the section shown in Figure 6a for the LAMMPS input base file. This section contains functionalities added by our group to handle the grid-MD atom interaction and D3-like pairwise vdW attractions for DFT-CES2. The parameters for the *bjdisp* pair_style in *base.in.lammps* should be appropriately defined. The corresponding input syntaxes are detailed in Figures S3−S5.

We further note that these input base files are not directly provided to QE or LAMMPS. Instead, the wrapper script, *qmmm_dftces2.sh* (included in the Supporting Information) refers to these files to generate the actual input files for QE and LAMMPS on the fly. Therefore, the locations of the input base files must be specified in the header section of the script.

(Step 3) Setting up the Simulation Protocol for QM/MD Iterations. The wrapper script automates the QM/MD iterations by generating inputs for QE and LAMMPS, executing the programs sequentially, and postprocessing the outputs using custom scripts for subsequent QM or MD runs. Simulation control parameters are defined as global variables in the header of the wrapper script, with annotations explaining their meanings (refer to *qmmm_dftces2.sh* in the Supporting Information).

Important input variables for new DFT-CES2 simulations include:

- ${QMMMINISTEP} and ${QMMMFINSTEP} − Define the number of QM and MD iterations based on their difference.
- ${ECONV} − Energy convergence criterion for the DFT-CES2 iterations, with the unit in kcal/mol (default: 0.1)
- ${SUPERCELL} − Specifies the number of QM cell repetitions needed to match the MD cell
- ${LAMMPS} − Path to LAMMPS executable
- ${QEPW} and ${QEPP} − Path to QE executables
- ${QMLMPTYPE} − A user-defined array that assigns atom types, as defined in the LAMMPS base input file, to atoms in the QM region. In this example, atom type 3 corresponds to a carbon atom in the QM region.
- ${LAMMPSRESTART} − The filename for the restart file, which stores the initial structural information. The wrapper script parses this file and partitions the total system into QM and MM regions. To distinguish the atoms in the QM region, ${QMLMPTYPE} must be properly configured.

Additionally, the wrapper script defines a_b and α_b^{iso} in Table 1 using the arrays of ${ATOMrepA} and ${ATOMalpha}. It also appends the parts shown in Figure 6b to the QE input file, specifying the filenames for the grid data: $\langle v_{Pauli}(\boldsymbol{r})\rangle$ and $\langle v_q^B(\boldsymbol{r})\rangle + \langle v_{bq}(\boldsymbol{r})\rangle$.

(Step 4) Execution of the Wrapper Script. When *qmmm_dftces2.sh* is executed, it first performs DFT optimization in vacuum. Then, it calls the LAMMPS module to run an MD simulation, sampling ensemble-averaged potentials that influence the subsequent DFT optimization.

https://doi.org/10.1021/jacsau.5c00176
JACS Au 2025, 5, 2047−2058

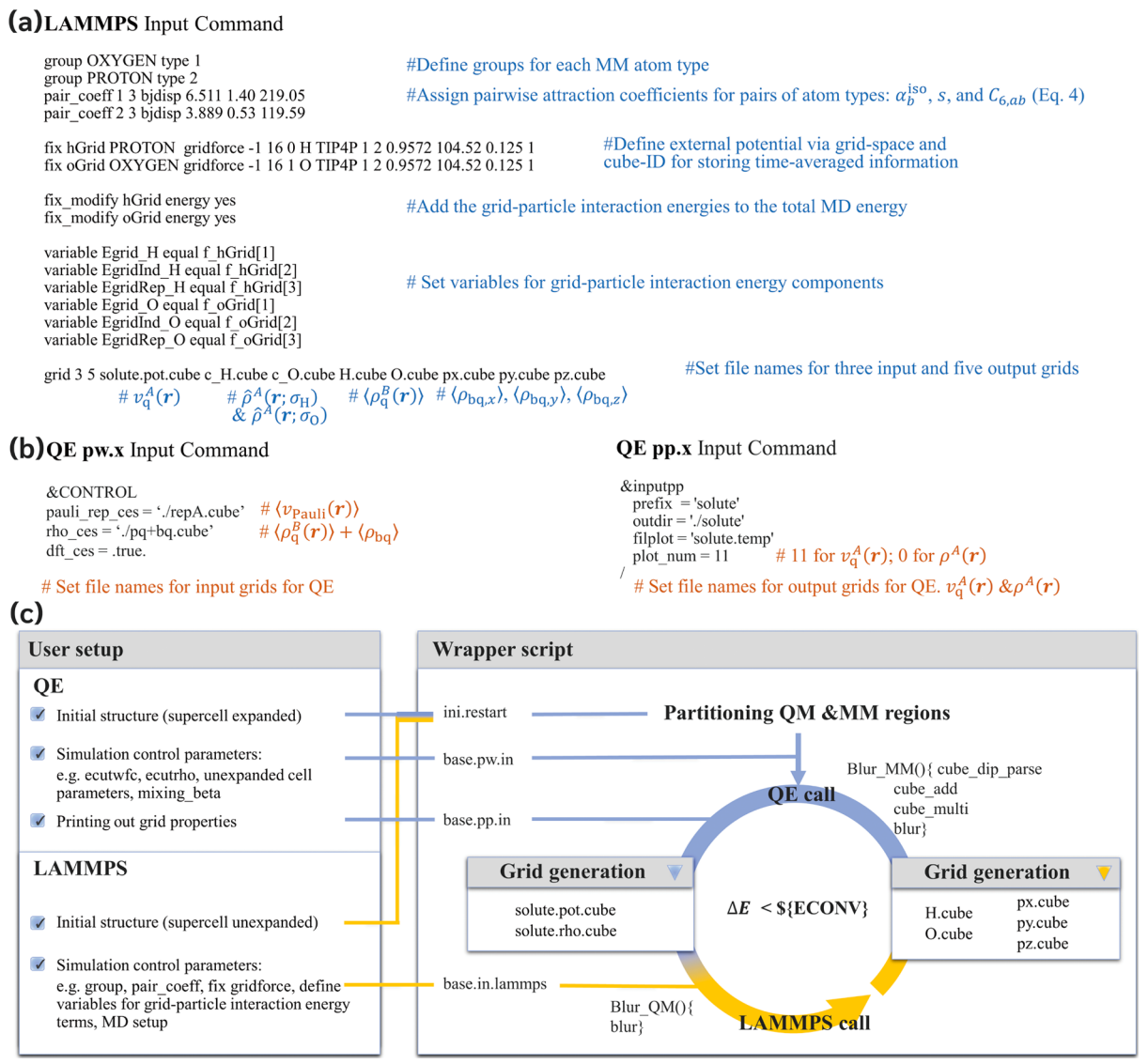

Figure 6. Example of input files for DFT-CES2 and overall simulation scheme. (a) Key sections added to the LAMMPS input file. (b) Key sections included in the QE input file. (c) A schematic summarizing the parts requiring user input and how the wrapper scripts perform DFT-CES2.

During these iterations, the structure and electron density of the QM system are updated, while the ensemble-averaged potentials are refined through MD simulations. This process continues until the convergence criterion is met or the maximum number of iterations is reached (Figure 6c).

CONCLUSION

We developed a quantum-mechanics-based embedding scheme for mean-field QM/MM and introduced a new simulation method called DFT-CES2 based on it. DFT-CES2 effectively describes the quantum-mechanical Pauli repulsion arising from wave function (or electron density) overlap between the QM and MM regions. Additionally, it accounts for dispersion attraction using Grimme's D3 method, as well as both first- and second-order electrostatics within the mean-field coupling framework.

To describe Pauli repulsion, DFT-CES2 requires an atom-species-dependent repulsion parameter, a_b. It also requires predefined atomic polarizabilities to model not only the second-order induction energy but also the size of the electron density of atoms in the MM region. By utilizing high-level quantum mechanical energies, we systematically optimized the required parameters, and demonstrated that they can describe non-covalent intermolecular interactions with quasi-chemical accuracy to reliably predict complex surface water interactions and contact angles.

Based on an appropriate energy partitioning and universally optimized atom-dependent parameters, DFT-CES2 is expected to be applicable to investigate complex solid−liquid interfaces without requiring additional heavy system-dependent parametrization. In addition to the surface wettability demonstrated in this study, DFT-CES2 is anticipated to have broad applicability in research areas such as heterogeneous catalytic reactions, electrochemical interfaces, semiconductor-liquid interfaces, and beyond.

ASSOCIATED CONTENT

Data Availability Statement

github.com/dft-ces/dft-ces2

https://doi.org/10.1021/jacsau.5c00176
JACS Au 2025, 5, 2047−2058

Supporting Information

The Supporting Information is available free of charge at https://pubs.acs.org/doi/10.1021/jacsau.5c00176.

Notes on the derivations of mean atomic forces for DFT optimization and external forces on MM particles, error estimations, atom-dependent repulsion parametrization details, computational details, and coupling of alchemical free energy method to DFT-CES2; figures illustrating linear correlation relating R_{ab}^{0} to atomic polarizability, distribution of a point charge to grid points, syntax examples of new commands for DFT-CES2, header structure of the wrapper script, atomic polarizabilities of individual atoms in transition metal oxides, optimizations of atom-dependent repulsion parameters for N, S, alkali metal ions, halide ions, and rare gas atoms, optimization of scaling parameters for dispersion energy, comparison of DFT-CES2 energy with CCSD(T) binding energy for alkali metal ions, halide ions, and rare gas atoms, benchmarks of hydrogen bonded dimer interactions, DFT cells for oxide systems, and thermodynamic integration results for various oxide-water systems; tables of comparisons between nonorthgonalized and approximately orthgonalized wave functions, benchmarks of DFT-CES2 molecular interaction energies (using A24, S22, water interaction sets), performance comparisons of DFT-CES2 energies with other QM/MM methods, and benchmarks of molecule adsorption energies on metals and graphene; compressed example file for DFT-CES2 simulations (PDF)

Examples of input files and wrapper script (ZIP)

AUTHOR INFORMATION

Corresponding Author

Hyungjun Kim − *Department of Chemistry, Korea Advanced Institute of Science and Technology (KAIST), Yuseong-gu, Daejeon 34141, Republic of Korea;* orcid.org/0000-0001-8261-9381; Email: linus16@kaist.ac.kr

Authors

Taehwan Jang − *Department of Chemistry, Korea Advanced Institute of Science and Technology (KAIST), Yuseong-gu, Daejeon 34141, Republic of Korea;* orcid.org/0000-0001-9076-7202

Seung-Jae Shin − *School of Energy and Chemical Engineering, Ulsan National Institute of Science and Technology (UNIST), Ulsan 44919, Republic of Korea;* orcid.org/0000-0002-5530-4453

Hyung-Kyu Lim − *Division of Chemical Engineering and Bioengineering, Kangwon National University, Chuncheon 24341, Republic of Korea;* orcid.org/0000-0002-2403-2766

William A. Goddard, III − *Materials and Process Simulation Center, California Institute of Technology, Pasadena, California 91125, United States;* orcid.org/0000-0003-0097-5716

Complete contact information is available at: https://pubs.acs.org/10.1021/jacsau.5c00176

Funding

This work was supported by the National Research Foundation of Korea (NRF), grants funded by the Korean government (MSIT) (Nos. 2021R1A2C2009643, RS-2024-00405261 and RS-2024-00450102).

Notes

The authors declare no competing financial interest.

ACKNOWLEDGMENTS

The authors express gratitude for supercomputing resources provided by the Korea Institute of Science and Technology Information (KSC-2021-CRE-0277).

REFERENCES

(1) Bruix, A.; Margraf, J. T.; Andersen, M.; Reuter, K. First-principles-based multiscale modelling of heterogeneous catalysis. *Nat. Catal* **2019**, *2*, 659−670.

(2) Mathew, K.; Kolluru, V. S. C.; Mula, S.; Steinmann, S. N.; Hennig, R. G. Implicit self-consistent electrolyte model in plane-wave density-functional theory. *J. Chem. Phys.* **2019**, *151*, 234101.

(3) Shin, S.-J.; et al. On the importance of the electric double layer structure in aqueous electrocatalysis. *Nat. Commun.* **2022**, *13*, 174.

(4) Shin, S.-J.; et al. A unifying mechanism for cation effect modulating C1 and C2 productions from CO2 electroreduction. *Nat. Commun.* **2022**, *13*, 5482.

(5) Lin, H.; Truhlar, D. G. QM/MM: What have we learned, where are we, and where do we go from here? *Theor. Chem. Acc.* **2007**, *117*, 185−199.

(6) Faheem, M.; Heyden, A. Hybrid quantum mechanics/molecular mechanics solvation scheme for computing free energies of reactions at metal-water interfaces. *J. Chem. Theory Comput* **2014**, *10*, 3354−3368.

(7) Abidi, N.; Steinmann, S. N. An Electrostatically Embedded QM/MM Scheme for Electrified Interfaces. *ACS Appl. Mater. Interfaces* **2023**, *15*, 25009−25017.

(8) Lim, H. K.; Lee, H.; Kim, H. A Seamless Grid-Based Interface for Mean-Field QM/MM Coupled with Efficient Solvation Free Energy Calculations. *J. Chem. Theory Comput* **2016**, *12*, 5088−5099.

(9) Yamamoto, T. Variational and perturbative formulations of quantum mechanical/molecular mechanical free energy with mean-field embedding and its analytical gradients. *J. Chem. Phys.* **2008**, *129*, 244104.

(10) Zhang, Y.; Liu, H.; Yang, W. Free energy calculation on enzyme reactions with an efficient iterative procedure to determine minimum energy paths on a combined *ab initio* QM/MM potential energy surface. *J. Chem. Phys.* **2000**, *112*, 3483−3492.

(11) Galván, I. F.; Sánchez, M. L.; Martín, M. E.; Olivares del Valle, F. J.; Aguilar, M. A. ASEP/MD: A program for the calculation of solvent effects combining QM/MM methods and the mean field approximation. *Comput. Phys. Commun.* **2003**, *155*, 244−259.

(12) Rosta, E.; Haranczyk, M.; Chu, Z. T.; Warshel, A. Accelerating QM/MM free energy calculations: Representing the surroundings by an updated mean charge distribution. *J. Phys. Chem. B* **2008**, *112*, 5680−5692.

(13) Jang, T.; Paik, D.; Shin, S.; Kim, H. Density functional theory in classical explicit solvents: Mean-field QM/MM method for simulating solid-liquid interfaces. *Bull. Korean Chem. Soc.* **2022**, *43*, 476.

(14) Jorgensen, W. L.; Maxwell, D. S.; Tirado-Rives, J. Development and testing of the OPLS all-atom force field on conformational energetics and properties of organic liquids. *J. Am. Chem. Soc.* **1996**, *118*, 11225−11236.

(15) Lee, H.; Lim, H. K.; Kim, H. Hydration thermodynamics of non-polar aromatic hydrocarbons: Comparison of implicit and explicit solvation models. *Molecules* **2018**, *23*, 2927.

(16) Gim, S.; Lim, H. K.; Kim, H. Multiscale Simulation Method for Quantitative Prediction of Surface Wettability at the Atomistic Level. *J. Phys. Chem. Lett.* **2018**, *9*, 1750−1758.

(17) Gim, S.; Cho, K. J.; Lim, H.-K.; Kim, H. Structure, Dynamics, and Wettability of Water at Metal Interfaces. *Sci. Rep* **2019**, *9*, 14805.

(18) Cho, K. J.; Gim, S.; Lim, H. K.; Kim, C.; Kim, H. Water Slippage on Graphitic and Metallic Surfaces: Impact of the Surface Packing

Structure and Electron Density Tail. *J. Phys. Chem. C* **2020**, *124*, 11392−11400.
(19) Dohn, A. O.; et al. Grid-Based Projector Augmented Wave (GPAW) Implementation of Quantum Mechanics/Molecular Mechanics (QM/MM) Electrostatic Embedding and Application to a Solvated Diplatinum Complex. *J. Chem. Theory Comput* **2017**, *13*, 6010−6022.
(20) Laio, A.; VandeVondele, J.; Rothlisberger, U. A Hamiltonian electrostatic coupling scheme for hybrid Car-Parrinello molecular dynamics simulations. *J. Chem. Phys.* **2002**, *116*, 6941−6947.
(21) Cortona, P. Self-consistently determined properties of solids without band-structure calculations. *Phys. Rev. B* **1991**, *44*, 8454−8458.
(22) Wesolowski, T. A.; Warshel, A. Frozen Density Functional Approach for ab Initio Calculations of Solvated Molecules. *J. Phys. Chem.* **1993**, *97*, 8050−8053.
(23) Huang, C.; Pavone, M.; Carter, E. A. Quantum mechanical embedding theory based on a unique embedding potential. *J. Chem. Phys.* **2011**, *134*, 154110.
(24) Grimme, S.; Antony, J.; Ehrlich, S.; Krieg, H. A consistent and accurate *ab initio* parametrization of density functional dispersion correction (DFT-D) for the 94 elements H-Pu. *J. Chem. Phys.* **2010**, *132*, 154104.
(25) Johnson, E. R.; Becke, A. D. A post-Hartree-Fock model of intermolecular interactions: Inclusion of higher-order corrections. *J. Chem. Phys.* **2006**, *124*, 174104.
(26) Casimir, H. B. G.; Polder, D. The Influence of Retardation on the London-van der Waals Forces. *Phys. Rev.* **1948**, *73*, 360−372.
(27) Grimme, S.; Antony, J.; Ehrlich, S.; Krieg, H. A consistent and accurate ab initio parametrization of density functional dispersion correction (DFT-D) for the 94 elements H-Pu. *J. Chem. Phys.* **2010**, *132*, 154104.
(28) Grimme, S.; Ehrlich, S.; Goerigk, L. Effect of the damping function in dispersion corrected density functional theory. *J. Comput. Chem.* **2011**, *32*, 1456−1465.
(29) Fedorov, D. V.; Sadhukhan, M.; Stöhr, M.; Tkatchenko, A. Quantum-Mechanical Relation between Atomic Dipole Polarizability and the van der Waals Radius. *Phys. Rev. Lett.* **2018**, *121*, 183401.
(30) Jensen, J. H.; Gordon, M. S. An approximate formula for the intermolecular Pauli repulsion between closed shell molecules. *Mol. Phys.* **1996**, *89*, 1313−1325.
(31) Roothaan, C. C. J. New Developments in Molecular Orbital Theory. *Rev. Mod. Phys.* **1951**, *23*, 69−89.
(32) Boal, D. H.; Glosli, J. N. Quasiparticle model for nuclear dynamics studies: Ground-state properties. *Phys. Rev. C* **1988**, *38*, 1870−1878.
(33) Klakow, D.; Toepffer, C.; Reinhard, P.-G. Semiclassical molecular dynamics for strongly coupled Coulomb systems. *J. Chem. Phys.* **1994**, *101*, 10766−10774.
(34) Su, J. T.; Goddard, W. A. The dynamics of highly excited electronic systems: Applications of the electron force field. *J. Chem. Phys.* **2009**, *131*, 244501.
(35) Murrell, J. N.; Randić, M.; Williams, D. R. The theory of intermolecular forces in the region of small orbital overlap. *Proc. R Soc. A* **1965**, *284* (1399), 566−581.
(36) Salem, L. The forces between polyatomic molecules. II. Short-range repulsive forces. *Proc. R Soc. A* **1961**, *264* (1318), 379−391.
(37) Musher, J. I.; Salem, L. Energy of interaction between two molecules. *J. Chem. Phys.* **1966**, *44*, 2943−2946.
(38) Murrell, J. N.; Shaw, G. Intermolecular forces in the region of small orbital overlap. *J. Chem. Phys.* **1967**, *46*, 1768−1772.
(39) Rackers, J. A.; Ponder, J. W. Classical Pauli repulsion: An anisotropic, atomic multipole model. *J. Chem. Phys.* **2019**, *150*, 084104.
(40) Kim, Y. S.; Kim, S. K.; Lee, W. D. Dependence of the closed-shell repulsive interaction on the overlap of the electron densities. *Chem. Phys. Lett.* **1981**, *80*, 574−575.
(41) Mayer, A. Formulation in terms of normalized propagators of a charge-dipole model enabling the calculation of the polarization properties of fullerenes and carbon nanotubes. *Phys. Rev. B Condens Matter Mater. Phys.* **2007**, *75*, 27−29.
(42) Ponder, J. W.; et al. Current status of the AMOEBA polarizable force field. *J. Phys. Chem. B* **2010**, *114*, 2549−2564.
(43) Naserifar, S.; Goddard, W. A. The quantum mechanics-based polarizable force field for water simulations. *J. Chem. Phys.* **2018**, *149*, 174502.
(44) Babin, V.; Leforestier, C.; Paesani, F. Development of a 'first principles' water potential with flexible monomers: Dimer potential energy surface, VRT spectrum, and second virial coefficient. *J. Chem. Theory Comput* **2013**, *9*, 5395−5403.
(45) Giannozzi, P.; et al. QUANTUM ESPRESSO: A modular and open-source software project for quantum simulations of materials. *J. Phys.: Condens. Matter* **2009**, *21*, 395502.
(46) Plimpton, S. Fast Parallel Algorithms for Short-Range Molecular Dynamics. *J. Comput. Phys.* **1995**, *117*, 1.
(47) Bourke, P. Gaussian Cube Files. Available at www.paulbourke.net/dataformats/cube/. (Accessed: 1st October 2024).
(48) Gould, T.; Bučko, T. C6 Coefficients and Dipole Polarizabilities for All Atoms and Many Ions in Rows 1−6 of the Periodic Table. *J. Chem. Theory Comput* **2016**, *12*, 3603−3613.
(49) Gould, T.; Lebègue, S.; Ángyán, J. G.; Bučko, T. A Fractionally Ionic Approach to Polarizability and van der Waals Many-Body Dispersion Calculations. *J. Chem. Theory Comput* **2016**, *12*, 5920−5930.
(50) Grimme, S.; Antony, J.; Ehrlich, S.; Krieg, H. A consistent and accurate ab initio parametrization of density functional dispersion correction (DFT-D) for the 94 elements H-Pu. *J. Chem. Phys.* **2010**, *132*, 154104.
(51) Jurečka, P.; Šponer, J.; Černý, J.; Hobza, P. Benchmark database of accurate (MP2 and CCSD(T) complete basis set limit) interaction energies of small model complexes, DNA base pairs, and amino acid pairs. *Phys. Chem. Chem. Phys.* **2006**, *8*, 1985−1993.
(52) Řezáč, J.; Hobza, P. Describing noncovalent interactions beyond the common approximations: How accurate is the 'gold standard,' CCSD(T) at the complete basis set limit? *J. Chem. Theory Comput* **2013**, *9*, 2151−2155.
(53) Řezáč, J.; Riley, K. E.; Hobza, P. S66: A well-balanced database of benchmark interaction energies relevant to biomolecular structures. *J. Chem. Theory Comput* **2011**, *7*, 2427−2438.
(54) Řezáč, J.; Riley, K. E.; Hobza, P. Benchmark calculations of noncovalent interactions of halogenated molecules. *J. Chem. Theory Comput* **2012**, *8*, 4285−4292.
(55) Mezei, M. The finite difference thermodynamic integration, tested on calculating the hydration free energy difference between acetone and dimethylamine in water. *J. Chem. Phys.* **1987**, *86*, 7084−7088.
(56) Vega, C.; De Miguel, E. Surface tension of the most popular models of water by using the test-area simulation method. *J. Chem. Phys.* **2007**, *126*, 154707.
(57) Horn, H. W.; et al. Development of an improved four-site water model for biomolecular simulations: TIP4P-Ew. *J. Chem. Phys.* **2004**, *120*, 9665−9678.
(58) Morcos, I. Surface tension of stress-annealed pyrolytic graphite. *J. Chem. Phys.* **1972**, *57*, 1801−1802.
(59) Wang, S.; Zhang, Y.; Abidi, N.; Cabrales, L. Wettability and surface free energy of graphene films. *Langmuir* **2009**, *25*, 11078−11081.
(60) Fowkes, F. M.; Harkins, W. D. The State of Monolayers Adsorbed at the Interface Solid—Aqueous Solution. *J. Am. Chem. Soc.* **1940**, *62*, 3377−3386.
(61) Steinmann, S. N.; Michel, C. How to Gain Atomistic Insights on Reactions at the Water/Solid Interface? *ACS Catal.* **2022**, *12*, 6294−6301.
(62) Gim, S.; Lim, H. K.; Kim, H. Multiscale Simulation Method for Quantitative Prediction of Surface Wettability at the Atomistic Level. *J. Phys. Chem. Lett.* **2018**, *9*, 1750−1758.
(63) Nowak, E.; Combes, G.; Stitt, E. H.; Pacek, A. W. A comparison of contact angle measurement techniques applied to highly porous catalyst supports. *Powder Technol.* **2013**, *233*, 52−64.

https://doi.org/10.1021/jacsau.5c00176
JACS Au 2025, 5, 2047−2058

(64) He, W.; et al. Surface Modification on Solution Processable ZrO2 High-k Dielectrics for Low Voltage Operations of Organic Thin Film Transistors. *J. Phys. Chem. C* **2016**, *120*, 9949−9957.
(65) Wang, R.; et al. Light-induced amphiphilic surfaces. *Nature* **1997**, *388*, 431−432.
(66) Azimi, G.; Dhiman, R.; Kwon, H. M.; Paxson, A. T.; Varanasi, K. K. Hydrophobicity of rare-earth oxide ceramics. *Nat. Mater.* **2013**, *12*, 315−320.
(67) Fu, S. P.; et al. On the wetting behavior of ceria thin films grown by pulsed laser deposition. *Appl. Phys. Lett.* **2017**, *110*, 081601.

https://doi.org/10.1021/jacsau.5c00176
JACS Au 2025, 5, 2047−2058